

Comprehensive Nonlinear Modeling of a Miniature Unmanned Helicopter



Guowei Cai*
Research Scientist
Temasek Laboratories
National University of Singapore
Singapore



Ben M. Chen
Professor
Department of Electrical and Computer Engineering
National University of Singapore, Singapore



Tong H. Lee
Professor



Kai-Yew Lum
Associate Professor
Department of Electrical Engineering
National ChiNan University
Taiwan

A nonlinear flight dynamics model that can be adopted by small-scale unmanned aerial vehicle (UAV) helicopters is presented. To minimize structural complexity, the proposed nonlinear model contains only four essential components, i.e., kinematics, rigid-body dynamics, main rotor flapping dynamics, and yaw rate feedback controller dynamics. A five-step parameter determination procedure is proposed to estimate the unknown parameters of the flight dynamics model. Based on the time-domain evaluations conducted, the nonlinear model is proven to be accurate in capturing the flight dynamics of our UAV helicopter platform over a wide envelope.

Nomenclature

A_{b_s}	coupling effect of the bare main rotor flapping, s^{-1}
A_{lon}	linkage gain ratio of θ_{cyc, a_s} to δ_{lon} , rad
a_s	longitudinal tip-path-plane (TPP) flapping angle of the main rotor, with pitch-up positive, rad
B_{a_s}	coupling effect of the bare main rotor flapping, s^{-1}
B_{lat}	linkage gain ratio of θ_{cyc, b_s} to δ_{lat} , rad
b_{mr}	main rotor blade number
b_s	lateral TPP flapping angle of the main rotor, with roll-right positive, rad
b_{tr}	tail rotor blade number
C_{D0}	drag coefficient of the main rotor blade
C_{lon}	linkage gain ratio of stabilizer bar cyclic change to δ_{lon} , rad
$C_{l\alpha}$	lift curve slope, rad^{-1}
c_{mr}	main rotor blade chord length, m
c_s	longitudinal TPP flapping angle of the stabilizer bar, with pitch-up positive, rad
c_{sb}	stabilizer bar paddle chord length, m
c_{tr}	tail rotor chord length, m
D_{hf}	horizontal stabilizer location behind the center of gravity (CG), m
D_{lat}	linkage gain ratio of stabilizer bar cyclic change to δ_{lat} , rad
D_{tr}	tail rotor hub location behind the CG, m
D_{vf}	vertical stabilizer location behind the CG, m
d_s	lateral TPP flapping angle of the stabilizer bar, with roll-right positive, rad
e_{mr}	effective hinge offset of the main rotor, m

F_b	aerodynamic force vector, N
$F_{b,g}$	gravity force vector projected onto the body frame, N
H	vertical location relative to the CG, m
g	local acceleration of gravity, m/s^2
I	moment of inertia, $kg \cdot m^2$
J	moment of inertia matrix characterized by J_{xx} , J_{yy} , J_{zz} , $kg \cdot m^2$
J_{ave}	average cost function of CIFER frequency-domain estimation
K_a	ratio of yaw rate to normalized rudder input, rad/s
K_{col}	ratio of main rotor blade collective pitch to collective pitch servo input, rad
K_I	integral gain of the yaw rate feedback controller
K_P	proportional gain of the yaw rate feedback controller
K_{ped}	ratio of tail rotor blade collective pitch to rudder servo input, rad
K_{sb}	ratio of main rotor blade cyclic pitch to stabilizer bar TPP flapping
K_β	rotor spring constant, N·m
L	rolling moment, $kg \cdot m^2$
M	pitching moment, $kg \cdot m^2$
M_b	aerodynamic moment vector, $kg \cdot m^2$
m	helicopter mass, kg
N	yawing moment, $kg \cdot m^2$
n_{tr}	gear ratio of the tail rotor to the main rotor
P_c	climbing power of the main rotor, W
P_i	induced power of the main rotor, W
P_n	local NED (north–east–down) position characterized by x_n , y_n , z_n , ms
P_{pa}	parasitic power of the main rotor, W
P_{pr}	profile power of the main rotor, W
R_e	Reynolds number

*Corresponding author; email: tscaig@nus.edu.sg.

Manuscript received December 2009; accepted September 2011.

R_{mr}	main rotor blade radius, m
$R_{n/b}$	transformation matrix from the body to the local NED frames
$R_{sb,in}$	inner radius of the stabilizer bar disk, m
$R_{sb,out}$	outer radius of the stabilizer bar disk, m
R_{tr}	tail rotor blade radius, m
S	transformation matrix from $\omega_{b/n}^b$ to Euler angles derivatives
S	effective fuselage or airfoil area, m^2
T	thrust, N
V_a	velocity vector relative to the air, m/s
V_b	velocity vector expressed in the body frame, m/s
V_{wind}	wind velocity expressed in the body frame, m/s
v_i	induced velocity, m/s
v_{vf}	local airspeed at the vertical stabilizer, m/s
\hat{v}^2	intermediate variable in thrust calculation, m^2/s^2
w_{hf}	local vertical speed at the horizontal stabilizer, m/s
X, Y, Z	aerodynamic force along body-frame axis, N
α_{st}	critical angle of attack of stall, rad
γ	Lock number
γ_{xy}^2	coherence value
δ_{col}	normalized collective pitch servo input, $-1, 1$
δ_{lat}	normalized aileron servo input, $-1, 1$
δ_{lon}	normalized elevator servo input, $-1, 1$
δ_{ped}	normalized rudder servo input, $-1, 1$
$\delta_{ped,int}$	intermediate state in the yaw rate feedback controller
$\bar{\delta}_{ped}$	rudder servo actuator deflection, rad
θ_{col}	collective pitch angle of the main rotor blade, rad
$\theta_{cyc,as}$	longitudinal cyclic pitch of the main rotor blade, rad
$\theta_{cyc,bs}$	lateral cyclic pitch of the main rotor blade, rad
θ_{ped}	collective pitch angle of the tail rotor blade, rad
λ_{vf}	indicator of the vertical stabilizer expose to the tail rotor wake
ρ	air density, $kg \cdot m^{-3}$
τ	time constant, s
ϕ, θ, ψ	Euler angles, rad
Ω	rotating speed, rad/s
$\omega_{b/n}^b$	angular velocity vector characterized by p, q, r , rad/s

Subscripts

fus	fuselage
fx, fy, fz	body-frame x, y , and z directions
hf	horizontal stabilizer
mr	main rotor
sb	stabilizer bar
tr	tail rotor
vf	vertical stabilizer

Introduction

During the past two to three decades, small-scale unmanned aerial vehicle (UAV) helicopters have aroused great interest in the academic community. In the development of a small-scale UAV helicopter, flight dynamics modeling is an important and challenging step. A model that can accurately reflect the flight dynamics of a rotorcraft is necessary if one wishes to design a flight control system using advanced control techniques such as the linear quadratic regulator and the H_∞ control. As such, many researchers have put in great effort in flight dynamics modeling for small-scale UAV helicopters since the early 1990s. Successful results have been obtained based on both system identification and first-principles modeling approaches:

1) System identification is generally aimed at deriving a linearized model in certain flight condition or over a relatively narrow flight envelope. This method can be conducted in either time domain or frequency domain. On the one hand, in time-domain system identification, the linearized model is identified by matching predicted output responses against measured output responses in the time domain. Although it is challenging to apply time-domain system identification to identify an inherently unstable system such as a single-rotor helicopter (as discussed in Ref. 1), some successful results can be found in the literature, for example, Refs. 2 and 3. On the other hand, frequency-domain system identification determines the linearized model by minimizing the error between the model's frequency responses and those derived from measured time-domain data. This is more suitable for rotorcraft UAV modeling thanks to the following features: (i) efficient identification of unstable modes, (ii) easy elimination of noise, (iii) direct time-delay identification, and (iv) less intensive computation. Some successful results have been documented in Refs. 4–6.

2) First-principles modeling has been developed to obtain nonlinear models for full-scale rotorcrafts (manned and unmanned) over the full flight envelope. It is not popular for miniature UAV rotorcraft modeling, as it is generally labor intensive and requires estimation or measurement of the aerodynamic, inertial, and structural properties of the rotorcraft, as discussed in Ref. 1. Furthermore, first-principles models for full-scale helicopters (see, e.g., Refs. 7–9) commonly use high order and complex structures, with many parameters tuned iteratively based on the flight test data and existing databases. However, with the demand of predicting the flight dynamics of small-scale helicopters over the full envelope, first-principles modeling approach has gained strong interest in the past decade. Successful examples can be found in Refs. 10–12.

At the National University of Singapore, several miniature UAV helicopters have been constructed by the NUS UAV Research Team. They are upgraded from radio-controlled (RC) helicopters (of different sizes, weights, payloads, and flight endurance) by equipping them with our custom-developed avionic systems. Autonomous control laws have been designed for hover and near hover conditions using the linearized models obtained via system identification. To further explore the potential of our UAV helicopters, their flight dynamics over the full flight envelope have been studied and a minimum-complexity flight dynamics model has been derived. In what follows, the modeling work is introduced in details.

Structure of the Flight Dynamics Model

A key challenge in determining the structure of a flight dynamics model is that the model's structure directly affects both identifiability and validity. Furthermore, model's complexity should be minimized to ease practical control implementation. To achieve the best trade-off, an extensive study on the hybrid model structure introduced in Refs. 1 and 6 and related modeling work such as Refs. 3, 4, 10, and 12–18 has been carried out. The flight dynamics model thus obtained features minimum structural complexity and consists of only four key components: (1) kinematics, (2) six-degree-of-freedom (DOF) rigid-body dynamics, (3) main rotor flapping dynamics, and (4) yaw rate feedback controller dynamics. This model contains 15 states and 4 inputs, which are summarized in Table 1.

Kinematics

In the kinematic part, two Cartesian coordinate frames, i.e., the local NED (north-east-down) frame and the body frame, are used. Definitions of the origin and axes directions can be found in many texts, such as

Table 1. State and input variables of the flight dynamics model

Variable	Physical Description	Unit
$\mathbf{P}_n = (x_n \ y_n \ z_n)^T$	Position vector in local NED frame	m
$\mathbf{V}_b = (u \ v \ w)^T$	Local NED velocity projected onto the body frame	m/s
$\boldsymbol{\omega}_{b/n}^b = (p \ q \ r)^T$	Angular velocity (local NED frame w.r.t. body frame)	rad/s
ϕ, θ, ψ	Euler angles	rad
a_s, b_s	TPP flapping angles	rad
$\delta_{ped,int}$	Intermediate state of yaw rate feedback controller	NA
δ_{lat}	Normalized aileron servo input (-1, 1)	NA
δ_{lon}	Normalized elevator servo input (-1, 1)	NA
δ_{col}	Normalized collective pitch servo input (-1, 1)	NA
δ_{ped}	Normalized rudder servo input (-1, 1)	NA

Ref. 19. In our work, the local NED frame is assumed to be inertial. Both translational and rotational motions between these two frames are studied.

The translational motion is expressed by

$$\dot{\mathbf{P}}_n = \mathbf{V}_n = \mathbf{R}_{n/b} \mathbf{V}_b \quad (1)$$

where $\mathbf{R}_{n/b}$ is the rotation matrix and given by

$$\mathbf{R}_{n/b} = \begin{bmatrix} \mathbf{c}_\theta \mathbf{c}_\psi & \mathbf{s}_\phi \mathbf{s}_\theta \mathbf{c}_\psi - \mathbf{c}_\phi \mathbf{s}_\psi & \mathbf{c}_\phi \mathbf{s}_\theta \mathbf{c}_\psi + \mathbf{s}_\phi \mathbf{s}_\psi \\ \mathbf{c}_\theta \mathbf{s}_\psi & \mathbf{s}_\phi \mathbf{s}_\theta \mathbf{s}_\psi + \mathbf{c}_\phi \mathbf{c}_\psi & \mathbf{c}_\phi \mathbf{s}_\theta \mathbf{s}_\psi - \mathbf{s}_\phi \mathbf{c}_\psi \\ -\mathbf{s}_\theta & \mathbf{s}_\phi \mathbf{c}_\theta & \mathbf{c}_\phi \mathbf{c}_\theta \end{bmatrix} \quad (2)$$

where $\mathbf{s}_\star = \sin(\star)$ and $\mathbf{c}_\star = \cos(\star)$.

The rotational motion is described by

$$\begin{pmatrix} \dot{\phi} \\ \dot{\theta} \\ \dot{\psi} \end{pmatrix} = \mathbf{S} \boldsymbol{\omega}_{b/n}^b \quad (3)$$

where the lumped transformation matrix \mathbf{S} is given by

$$\mathbf{S} = \begin{bmatrix} 1 & \sin \phi \tan \theta & \cos \phi \tan \theta \\ 0 & \cos \phi & -\sin \phi \\ 0 & \sin \phi / \cos \theta & \cos \phi / \cos \theta \end{bmatrix} \quad (4)$$

Wind velocities (denoted by \mathbf{V}_{wind}) are projected into the body frame using

$$\mathbf{V}_a = \begin{pmatrix} u_a \\ v_a \\ w_a \end{pmatrix} = \begin{pmatrix} u - u_{wind} \\ v - v_{wind} \\ w - w_{wind} \end{pmatrix} \quad (5)$$

Rigid-body dynamics

The six-DOF rigid-body dynamics of the helicopter fuselage are represented by the following Newton–Euler equations:

$$\dot{\mathbf{V}}_b = -\boldsymbol{\omega}_{b/n}^b \times \mathbf{V}_b + \frac{\mathbf{F}_b}{m} + \frac{\mathbf{F}_{b,g}}{m} \quad (6)$$

and

$$\dot{\boldsymbol{\omega}}_{b/n}^b = \mathbf{J}^{-1} [\mathbf{M}_b - \boldsymbol{\omega}_{b/n}^b \times (\mathbf{J} \boldsymbol{\omega}_{b/n}^b)] \quad (7)$$

where \times denotes the cross product of two vectors, m is the helicopter mass, $\mathbf{J} = \text{diag}\{J_{xx}, J_{yy}, J_{zz}\}$ is the moment of inertia matrix (note that the off-axis moment of inertia is small and thus ignored), $\mathbf{F}_{b,g} = (-mg \mathbf{s}_\theta \ mg \mathbf{s}_\phi \mathbf{c}_\theta \ mg \mathbf{c}_\phi \mathbf{c}_\theta)^T$ is the vector of gravitational force, \mathbf{F}_b is the vector of aerodynamic force, and \mathbf{M}_b is the vector of

aerodynamic moment. The last two terms are given by

$$\mathbf{F}_b = \begin{pmatrix} X_{mr} + X_{fus} \\ Y_{mr} + Y_{fus} + Y_{tr} + Y_{vf} \\ Z_{mr} + Z_{fus} + Z_{hf} \end{pmatrix} \quad \text{and} \quad \mathbf{M}_b = \begin{pmatrix} L_{mr} + L_{vf} + L_{tr} \\ M_{mr} + M_{hf} \\ N_{mr} + N_{vf} + N_{tr} \end{pmatrix} \quad (8)$$

where $(\cdot)_{mr}$, $(\cdot)_{tr}$, $(\cdot)_{fus}$, $(\cdot)_{vf}$, and $(\cdot)_{hf}$ stand for main rotor, tail rotor, fuselage, vertical stabilizer, and horizontal stabilizer, respectively, which are the five sources of aerodynamic forces and moments. In what follows, the expressions of these force and moment terms are detailed. It should be highlighted that these expressions are mainly based on the results presented by Heffley and Mnich in Ref. 14. Some modifications have been performed to make the expressions suitable for small-scale helicopters.

Main rotor force and moment. The forces and moments generated by the main rotor are computed based on classical momentum theory, under the assumption of uniform inflow distribution. As introduced in Ref. 20, the momentum theory is an efficient global analysis regarding overall flow velocities, thrust, and power. As such, in our flight dynamics model, the thrust of the main rotor is modeled based on the momentum theory. Figure 1 shows a block diagram of main rotor thrust computation. This computation was first proposed by Heffley and Mnich (Ref. 14) and is partially modified to suit small-scale UAV helicopters. This process features a recursion scheme that is able to achieve quick convergence of two key terms: main rotor thrust T_{mr} and induced velocity $v_{i,mr}$, which are given by

$$T_{mr} = \frac{\rho \Omega_{mr} R_{mr}^2 C_{l\alpha,mr} b_{mr} c_{mr}}{4} (w_{bl,mr} - v_{i,mr}) \quad (9)$$

and

$$v_{i,mr}^2 = \sqrt{\left(\frac{\hat{v}_{mr}^2}{2}\right)^2 + \left(\frac{T_{mr}}{2\rho\pi R_{mr}^2}\right)^2} - \frac{\hat{v}_{mr}^2}{2} \quad (10)$$

where

$$\hat{v}_{mr}^2 = u_a^2 + v_a^2 + w_{r,mr}(w_{r,mr} - 2v_{i,mr}) \quad (11)$$

$$w_{r,mr} = w_a + a_s u_a - b_s v_a \quad (12)$$

$$w_{bl,mr} = w_{r,mr} + \frac{2}{3} \Omega_{mr} R_{mr} \theta_{col} \quad (13)$$

$$\theta_{col} = K_{col} \delta_{col} + \theta_{col,0} \quad (14)$$

ρ is local air density, Ω_{mr} is the rotation speed of the main rotor, R_{mr} is the radius of the main rotor disk, $C_{l\alpha,mr}$ is the lift curve slope of the main rotor blade, b_{mr} is the number of blades in the main rotor, c_{mr} is the chord length of the main rotor blade, $w_{bl,mr}$ is the net vertical velocity relative to the main rotor, \hat{v}_{mr}^2 is an intermediate variable in the main rotor thrust

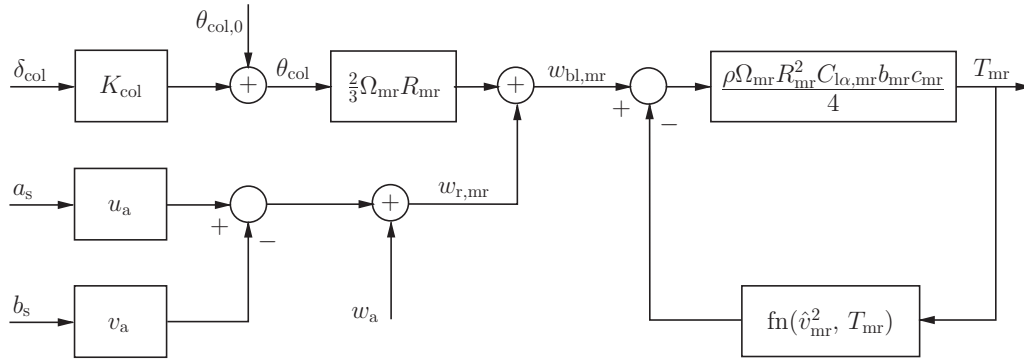


Fig. 1. Block diagram of main rotor thrust computation.

calculation, $w_{r,mr}$ is the net vertical velocity through the main rotor disk (note that this item includes main rotor flapping angles a_s and b_s , which will be addressed later), and θ_{col} is the collective pitch angle of the main rotor blade. It should be noted that the change of θ_{col} resulting from the collective pitch servo input δ_{col} is linear and can be expressed in terms of a scaling factor K_{col} and an offset value $\theta_{col,0}$ of the main-rotor collective pitch angle (when δ_{col} is zero).

Given a flight condition, the iteration scheme starts with the associated trim values of T_{mr} and $v_{i,mr}$. Furthermore, the iteration scheme runs for 10 loops in each computational process to obtain the converged results of T_{mr} and $v_{i,mr}$.

The force components generated by the main rotor are computed as follows:

$$\begin{aligned} X_{mr} &= -T_{mr} \sin a_s \\ Y_{mr} &= T_{mr} \sin b_s \\ Z_{mr} &= -T_{mr} \cos a_s \cos b_s \end{aligned} \quad (15)$$

The moments generated by the main rotor are given by

$$\begin{aligned} L_{mr} &= (K_\beta + T_{mr} H_{mr}) \sin(b_s) \\ M_{mr} &= (K_\beta + T_{mr} H_{mr}) \sin(a_s) \\ N_{mr} &= -P_{mr}/\Omega_{mr} \end{aligned} \quad (16)$$

Equations (15) and (16) reflect how the rotor flapping dynamics, which will be addressed later, are coupled with the rigid-body dynamics. The specific terms involved in the above force and moment expressions are K_β is the effective main rotor spring constant, H_{mr} is the main rotor hub location above the CG of the helicopter, and P_{mr} is the total power consumption that comprises (1) main rotor profile power P_{pr} , (2) main rotor induced power P_i , (3) parasitic power P_{pa} , and (4) climbing power P_c , i.e.,

$$P_{mr} = P_{pr} + P_i + P_{pa} + P_c \quad (17)$$

with

$$P_{pr} = \frac{\rho \Omega_{mr} R_{mr}^2 C_{D0} b_{mr} c_{mr}}{8} [(\Omega_{mr} R_{mr})^2 + 4.6(u_a^2 + v_a^2)] \quad (18)$$

$$P_i = T_{mr} v_{i,mr} \quad (19)$$

$$P_{pa} = |X_{fus} u_a| + |Y_{fus} v_a| + |Z_{fus}(w_a - v_{i,mr})| \quad (20)$$

and

$$P_c = \begin{cases} -m g w_a, & \text{if } w_a < 0 \\ 0, & \text{if } w_a \geq 0 \end{cases} \quad (21)$$

Note that in Eq. (18) C_{D0} is the drag coefficient of the main rotor blade, and X_{fus} , Y_{fus} , and Z_{fus} in Eq. (20) are the fuselage drag forces, which will be addressed later.

Tail rotor force and moment. For the tail rotor, its thrust T_{tr} and induced velocity $v_{i,tr}$ can be calculated using a similar 10-loop recursive scheme. Here the flapping effect is negligible due to the small size of the tail rotor blades and thus the recursive procedure is modified as follows:

$$T_{tr} = \frac{\rho \Omega_{tr} R_{tr}^2 C_{l\alpha,tr} b_{tr} c_{tr}}{4} (w_{bl,tr} - v_{i,tr}) \quad (22)$$

and

$$v_{i,tr}^2 = \sqrt{\left(\frac{\hat{v}_{tr}^2}{2}\right)^2 + \left(\frac{T_{tr}}{2\rho\pi R_{tr}^2}\right)^2} - \frac{\hat{v}_{tr}^2}{2} \quad (23)$$

where

$$\hat{v}_{tr}^2 = (w_a + q D_{tr})^2 + u_a^2 + w_{r,tr}(w_{r,tr} - 2v_{i,tr}) \quad (24)$$

$$w_{r,tr} = v_a - r D_{tr} + p H_{tr} \quad (25)$$

$$w_{bl,tr} = w_{r,tr} + \frac{2}{3} \Omega_{tr} R_{tr} \theta_{ped} \quad (26)$$

$$\theta_{ped} = K_{ped} \bar{\delta}_{ped} + \theta_{ped,0} \quad (27)$$

Ω_{tr} , R_{tr} , $C_{l\alpha,tr}$, b_{tr} , c_{tr} , $w_{bl,tr}$, \hat{v}_{tr}^2 , $w_{r,tr}$, H_{tr} , and θ_{ped} have the same physical meanings as their aforementioned counterparts of the main rotor, and D_{tr} is the tail rotor hub location behind the CG. The relationship between θ_{ped} and the rudder servo actuator deflection $\bar{\delta}_{ped}$ is also linear and is denoted by a scaling factor K_{ped} and an offset value $\theta_{ped,0}$ of the tail-rotor collective pitch angle (when $\bar{\delta}_{ped}$ is zero). It should be highlighted that in the above linear relationship the input is $\bar{\delta}_{ped}$ instead of δ_{ped} , due to the existence of the yaw rate feedback controller (to be addressed later).

The force component Y_{tr} is then given by

$$Y_{tr} = -T_{tr} \quad (28)$$

Since all our custom-built UAV helicopters have clockwise rotating main rotors (as seen from the top view), Y_{tr} is negative according to the body-frame definition.

The above tail rotor force generates two moments, i.e., L_{tr} and N_{tr} . The first component is caused by the vertical distance between the helicopter CG and the tail rotor hub, and the latter is responsible for countering the torque N_{mr} generated by the main rotor. They are given by

$$L_{tr} = Y_{tr} H_{tr} \quad \text{and} \quad N_{tr} = -Y_{tr} D_{tr} \quad (29)$$

Fuselage forces. The fuselage causes drag along the three body-frame directions during flight. As introduced in Ref. 10, in the computation of drag forces along the horizontal directions, the deflection of the main rotor downwash due to u_a and v_a should be considered. The fuselage is considered as a three-dimensional virtual flat plate, and the drag forces

are represented by the following quadratic form:

$$X_{\text{fus}} = \begin{cases} -\frac{\rho}{2} S_{fx} u_a v_{i,\text{mr}}, & \text{if } |u_a| \leq v_{i,\text{mr}} \\ -\frac{\rho}{2} S_{fx} u_a |u_a|, & \text{if } |u_a| > v_{i,\text{mr}} \end{cases} \quad (30)$$

$$Y_{\text{fus}} = \begin{cases} -\frac{\rho}{2} S_{fy} v_a v_{i,\text{mr}}, & \text{if } |v_a| \leq v_{i,\text{mr}} \\ -\frac{\rho}{2} S_{fy} v_a |v_a|, & \text{if } |v_a| > v_{i,\text{mr}} \end{cases} \quad (31)$$

where S_{fx} and S_{fy} are the effective drag area along the body-frame X and Y axes, respectively.

In the vertical direction, the fuselage is constantly exposed to the main rotor downwash. A uniform quadratic equation is used to express the vertical fuselage drag force Z_{fus} :

$$Z_{\text{fus}} = -\frac{\rho}{2} S_{fz} (w_a - v_{i,\text{mr}}) |w_a - v_{i,\text{mr}}| \quad (32)$$

where S_{fz} is the effective drag area along the body-frame Z axis.

Since our UAV helicopters are mechanically symmetrical by construction, the fuselage moments are very small. As such, they are not included in the flight dynamics model.

Vertical stabilizer force and moment. The vertical stabilizer is used to enhance stability in the yawing motion. For the side force computation, the following four points should be noted: (1) the side force arising from the camber of the vertical stabilizer is sufficiently small and thus not considered; (2) since the mounting position of the vertical stabilizer affects the local lateral airspeed v_{vf} , a parameter λ_{vf} is defined to indicate whether the vertical stabilizer is exposed to tail rotor wake ($\lambda_{\text{vf}} = 1$ if the vertical stabilizer is exposed to the tail rotor, otherwise $\lambda_{\text{vf}} = 0$); (3) the stall effect is considered, and the threshold condition is determined by the critical angle of attack (α_{st}); and (4) in stall, it is assumed that the side force is caused only by the dynamic pressure perpendicular to the vertical stabilizer. The local lateral airspeed at the vertical stabilizer is defined by

$$v_{\text{vf}} = v_a - r D_{\text{vf}} - \lambda_{\text{vf}} v_{i,\text{tr}} \quad (33)$$

where D_{vf} is the vertical stabilizer location behind the CG. The vertical stabilizer force is then given by

$$Y_{\text{vf}} = \begin{cases} -\frac{\rho}{2} C_{l\alpha,\text{vf}} S_{\text{vf}} v_{\text{vf}} |u_a|, & \text{if } \left| \frac{v_{\text{vf}}}{u_a} \right| \leq \tan(\alpha_{\text{st}}) \\ -\frac{\rho}{2} S_{\text{vf}} v_{\text{vf}} |v_{\text{vf}}|, & \text{if } \left| \frac{v_{\text{vf}}}{u_a} \right| > \tan(\alpha_{\text{st}}) \text{ (surface stalled)} \end{cases} \quad (34)$$

where $C_{l\alpha,\text{vf}}$ is the lift curve slope of the vertical stabilizer and S_{vf} is the area of the vertical stabilizer.

Similar to the tail rotor, the vertical stabilizer generates two moment components L_{vf} and N_{vf} along the X axis and Z axis of the body frame, respectively. They are given by

$$L_{\text{vf}} = Y_{\text{vf}} H_{\text{vf}} \quad \text{and} \quad N_{\text{vf}} = -Y_{\text{vf}} D_{\text{vf}} \quad (35)$$

where H_{vf} is the vertical stabilizer location above the CG.

Horizontal stabilizer force and moment. The horizontal stabilizer is designed to provide additional pitch stability. Its force computation is quite similar to that of the vertical stabilizer. It is noted that (1) the minor force component arising from the camber of the horizontal stabilizer is omit-

ted; (2) for our helicopters, the horizontal stabilizer is fully immersed in the main rotor downwash, which should be considered when computing the local vertical airspeed at the horizontal stabilizer w_{hf} ; and (3) the critical angle of attack α_{st} is identical with its counterpart for the vertical stabilizer since both stabilizers share similar size and shape. w_{hf} is given by

$$w_{\text{hf}} = w_a + q D_{\text{hf}} - v_{i,\text{mr}} \quad (36)$$

where D_{hf} is the horizontal stabilizer location behind the CG. The horizontal stabilizer force is given by

$$Z_{\text{hf}} = \begin{cases} -\frac{\rho}{2} C_{l\alpha,\text{hf}} S_{\text{hf}} w_{\text{hf}} |u_a|, & \text{if } \left| \frac{w_{\text{hf}}}{u_a} \right| \leq \tan(\alpha_{\text{st}}) \\ -\frac{\rho}{2} S_{\text{hf}} w_{\text{hf}} |w_{\text{hf}}|, & \text{if } \left| \frac{w_{\text{hf}}}{u_a} \right| > \tan(\alpha_{\text{st}}) \text{ (surface stalled)} \end{cases} \quad (37)$$

where $C_{l\alpha,\text{hf}}$ is the lift curve slope of the horizontal stabilizer and S_{hf} is the area of the horizontal stabilizer. The moment generated by Z_{hf} is computed by

$$M_{\text{hf}} = Z_{\text{hf}} D_{\text{hf}} \quad (38)$$

Main rotor flapping dynamics

The flapping of the main rotor is described by the tip-path-plane (TPP) equations of motion. It should be noted that RC helicopters generally feature a coupling between the fuselage inertia response and the main rotor flapping response, which is mainly due to the presence of a stabilizer bar. In our model, the effect of the stabilizer bar is lumped into the bare main rotor disk's flapping motion. The feasibility of such a simplification has been studied in some successful work such as Refs. 4 and 12.

Stabilizer bar dynamics. The stabilizer bar consists of a steel rod and two plastic paddles, which act as small aerodynamic surfaces. It is attached to main rotor shaft via a free-teetering hinge and can be regarded as a second rotor. The primary function of the stabilizer bar is to provide enhanced stability to ease manual control and to reduce the effect of wind gust or turbulence. The longitudinal and lateral TPP flapping angles of the stabilizer bar disk are defined as c_s (pitch-up positive) and d_s (roll-right positive), respectively. As introduced in Ref. 6, the flapping dynamics (from the cyclic pitch motion of the stabilizer bar paddle to the flapping angles) can be represented by two coupled, first-order differential equations

$$\begin{aligned} \dot{c}_s &= -q - \frac{1}{\tau_{\text{sb}}} c_s + \frac{C_{l\text{lon}}}{\tau_{\text{sb}}} \delta_{\text{lon}} \\ \dot{d}_s &= -p - \frac{1}{\tau_{\text{sb}}} d_s + \frac{D_{\text{lat}}}{\tau_{\text{sb}}} \delta_{\text{lat}} \end{aligned} \quad (39)$$

where $C_{l\text{lon}}$ (D_{lat}) is the ratio of stabilizer bar longitudinal (lateral) cyclic pitch to servo input δ_{lon} (δ_{lat}), τ_{sb} is the rotor flapping time constant of the stabilizer bar and defined by

$$\tau_{\text{sb}} = \frac{16}{\gamma_{\text{sb}} \Omega_{\text{mr}}} \quad (40)$$

where γ_{sb} is the stabilizer bar Lock number and given as

$$\gamma_{\text{sb}} = \frac{\rho c_{\text{sb}} C_{l\alpha,\text{sb}} (R_{\text{sb,out}}^4 - R_{\text{sb,in}}^4)}{I_{\beta,\text{sb}}} \quad (41)$$

Here c_{sb} is the chord length of the stabilizer bar paddle, $C_{l\alpha,\text{sb}}$ is the lift curve slope of the paddle, $R_{\text{sb,out}}$ and $R_{\text{sb,in}}$ are the outer and inner radiuses of the stabilizer bar rotor disk, and $I_{\beta,\text{sb}}$ is the moment of inertia

of the paddle, with the rotation axis coinciding with the main rotor shaft. It should be noted that, owing to the free-teetering feature, there is no coupling effect between the longitudinal and lateral flapping motions.

Bare main rotor. The longitudinal and lateral TPP flapping angles of the bare main rotor are defined as a_s (pitch-up positive) and b_s (roll-right positive), respectively. Following Ref. 6, the bare main rotor flapping dynamics (from the cyclic pitch motion of the main rotor blade to the rotor disk flapping angle) is expressed by

$$\begin{aligned} \dot{a}_s &= -q - \frac{1}{\tau_{mr}} a_s + A_{bs} b_s + \frac{1}{\tau_{mr}} \theta_{cyc,as} \\ \dot{b}_s &= -p + B_{as} a_s - \frac{1}{\tau_{mr}} b_s + \frac{1}{\tau_{mr}} \theta_{cyc,bs} \end{aligned} \quad (42)$$

with the involved parameters explained as follows:

1) τ_{mr} is the time constant of the main rotor flapping motion. As introduced in Ref. 21, for a nonteetering rotor, the time constant computation is expressed by

$$\tau_{mr} = \frac{16}{\gamma_{mr} \Omega_{mr}} \left(1 - \frac{8e_{mr}}{3R_{mr}} \right)^{-1} \quad (43)$$

where e_{mr} is the effective hinge offset of the main rotor and γ_{mr} is the main rotor blade Lock number given by

$$\gamma_{mr} = \frac{\rho c_{mr} C_{l\alpha, mr} R_{mr}^4}{I_{\beta, mr}} \quad (44)$$

where $I_{\beta, mr}$ is the moment of inertia of the main rotor blade with the rotation axis at the main shaft.

2) $\theta_{cyc,as}$ and $\theta_{cyc,bs}$ are the longitudinal and lateral cyclic pitch angles of the main rotor blade, respectively, and are given by

$$\begin{aligned} \theta_{cyc,as} &= A_{lon} \delta_{lon} + K_{sb} c_s \\ \theta_{cyc,bs} &= B_{lat} \delta_{lat} + K_{sb} d_s \end{aligned} \quad (45)$$

which indicates how the stabilizer bar affects the main rotor flapping motion. The cyclic pitch is driven by both the servo input (coming from the swash plate) and the stabilizer bar flapping angle, which is realized by a Bell–Hiller mixer. Note that the mechanical structure of the Bell–Hiller mixer determines the following three parameters: A_{lon} (a ratio of $\theta_{cyc,as}$ to δ_{lon}), B_{lat} (a ratio of $\theta_{cyc,bs}$ to δ_{lat}), and K_{sb} (a ratio of the main rotor blade cyclic pitch to the stabilizer bar flapping motion).

3) A_{bs} and B_{as} represent the coupling effect between longitudinal and lateral flapping motions. According to Ref. 6, their theoretical expressions are given by

$$A_{bs} = -B_{as} = \frac{8K_{\beta}}{\gamma_{mr} \Omega^2 I_{\beta}} \quad (46)$$

However, Eq. (46) generally does not agree with results obtained in practical flight test. The values of these two parameters will be further tuned based on flight test data.

Complete main rotor flapping dynamics. To derive the complete main rotor flapping dynamics, the above two TPP flapping dynamics are integrated together via the following three steps: (1) apply Laplace transform to Eqs. (39) and (42), (2) insert $c_s(s)$ and $d_s(s)$ into the expressions of $a_s(s)$ and $b_s(s)$, and (3) perform inverse Laplace transform, ignoring the items related to \dot{p} , \dot{q} , $\dot{\delta}_{lat}$, and $\dot{\delta}_{lon}$. The complete main rotor flapping dynamics are

$$\dot{a}_s = -\frac{\tau_{mr} + K_{sb} \tau_{sb}}{\tau_{mr} + \tau_{sb}} q - \frac{1}{\tau_{mr} + \tau_{sb}} a_s + \frac{\tau_{mr} A_{bs}}{\tau_{mr} + \tau_{sb}} b_s + \frac{A_{lon} + K_{sb} C_{lon}}{\tau_{mr} + \tau_{sb}} \delta_{lon} \quad (47)$$

and

$$\dot{b}_s = -\frac{\tau_{mr} + K_{sb} \tau_{sb}}{\tau_{mr} + \tau_{sb}} p + \frac{\tau_{mr} B_{as}}{\tau_{mr} + \tau_{sb}} a_s - \frac{1}{\tau_{mr} + \tau_{sb}} b_s + \frac{B_{lat} + K_{sb} D_{lat}}{\tau_{mr} + \tau_{sb}} \delta_{lat} \quad (48)$$

which are to be used to form the complete flight dynamics model.

Yaw rate feedback controller

Yaw control is challenging on RC helicopters as the yawing moment is extremely sensitive and difficult for human pilots to control. Nowadays almost all available RC helicopter products are equipped with a yaw rate feedback controller, which consists of a gyro sensor and a feedback controller to improve yaw damping, thus facilitating human pilots in controlling the yaw rate and the heading angle. Ideally, these components should be removed in the unmanned rotorcraft systems. They are, however, commonly preserved to ease backup manual control. As such, the dynamics of the yaw rate feedback controller should be considered.

The framework of the yaw rate feedback controller is depicted in Fig. 2. The joystick input signal, δ_{ped} , is amplified (by a factor of K_a) by a proportional amplifier circuit, which is then compared with the feedback yaw angular velocity r measured by the yaw rate gyro. The resulting difference is then sent to the embedded controller to generate the tail rotor servo deflection $\bar{\delta}_{ped}$. The yaw rate feedback controllers that are equipped in our UAV helicopters can be modeled as a PI compensator and is expressed by

$$\bar{\delta}_{ped} = \left(K_P + \frac{K_I}{s} \right) (K_a \delta_{ped} - r) \quad (49)$$

where K_P and K_I are the proportional and integral gains of the embedded controller. Defining an intermediate state $\delta_{ped,int}$, which is the integral

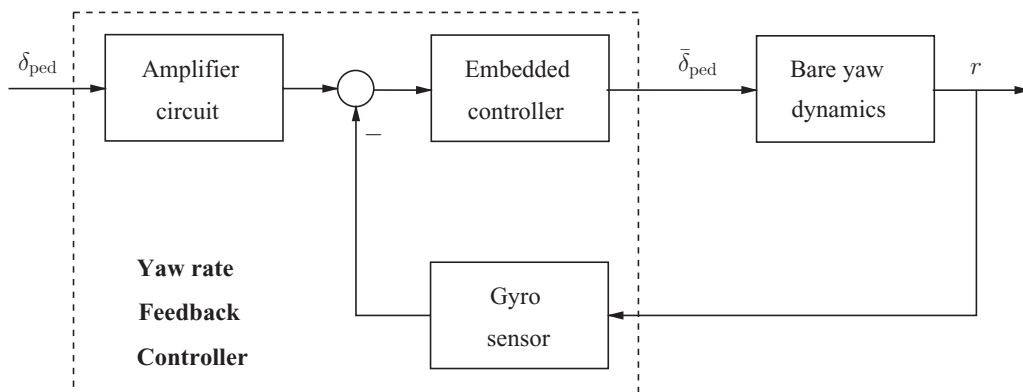


Fig. 2. Configuration of the yaw channel.

Table 2. Parameters determined via direct measurement

Parameter	Physical Meaning
$I_{\beta, mr} = 0.055 \text{ kg}\cdot\text{m}^2$	Moment of inertia of main rotor blade w.r.t. rotor hub
$I_{\beta, sb} = 0.004 \text{ kg}\cdot\text{m}^2$	Moment of inertia of stabilizer bar w.r.t. rotor hub
$R_{mr} = 0.705 \text{ m}$	Main rotor radius
$R_{sb, in} = 0.231 \text{ m}$	Stabilizer bar inner radius
$R_{sb, out} = 0.312 \text{ m}$	Stabilizer bar outer radius
$R_{tr} = 0.128 \text{ m}$	Tail rotor radius
$S_{fx} = 0.103 \text{ m}^2$	Effective longitudinal fuselage drag area
$S_{fy} = 0.900 \text{ m}^2$	Effective lateral fuselage drag area
$S_{fz} = 0.084 \text{ m}^2$	Effective vertical fuselage drag area
$S_{hf} = 0.011 \text{ m}^2$	Horizontal stabilizer area
$S_{vf} = 0.007 \text{ m}^2$	Vertical stabilizer area
$b_{mr} = 2$	Main rotor blade number
$b_{tr} = 2$	Tail rotor blade number
$c_{mr} = 0.062 \text{ m}$	Main rotor blade chord length
$c_{sb} = 0.059 \text{ m}$	Stabilizer bar chord length
$c_{tr} = 0.029 \text{ m}$	Tail rotor chord length
$e_{mr} = 0.07 \text{ m}$	Effective hinge offset of the main rotor
$g = 9.781 \text{ N}\cdot\text{kg}^{-1}$	Acceleration of gravity
$m = 9.750 \text{ kg}$	Helicopter mass
$n_{tr} = 4.650$	Gear ratio of the tail rotor to the main rotor
$\Omega_{mr} = 193.73 \text{ rad}$	Main rotor rotating speed
$\Omega_{tr} = 900.85 \text{ rad}$	Main rotor rotating speed
$\rho = 1.290 \text{ kg}/\text{m}^3$	Air density

of the error between the amplified yaw channel input signal and the yaw rate feedback, Eq. (49) can then be rewritten as

$$\begin{aligned} \delta_{ped, int} &= K_a \delta_{ped} - r \\ \bar{\delta}_{ped} &= K_P (K_a \delta_{ped} - r) + K_I \delta_{ped, int} \end{aligned} \quad (50)$$

Parameter Determination

In this section, a parameter determination method that corresponds to the above flight dynamics model is presented. The procedure includes five steps: (1) direct measurement, (2) ground test, (3) estimation based

on wind tunnel data, (4) flight test, and (5) fine-tuning. In what follows, it is applied to one of our miniature UAV helicopters, named HeLion, to determine the associated parameters.

Direct measurement

The first step focuses on the parameters that can be directly measured via observation or using simple devices (such as ruler and scale). Parameters belonging to this group are listed in Table 2. Note that I_{mr} and I_{sb} are computed based on the mass values of the main rotor blade and stabilizer bar (m_{mr} and m_{sb}). The equation used for moment of inertia calculation can be easily found in many physics texts.

Ground tests

A series of ground tests have been performed, which include (1) CG location determination, (2) measurement of moment of inertia, (3) airfoil deflection test, and (4) collective pitch curve examination.

CG location determination. The CG location experiment is repeated at least three times. Each time HeLion is suspended from an arbitrarily selected point. The suspension points are located at the main rotor hub, fuselage nose, and left of fuselage, respectively. The general idea is that the intersection of these three (or more) suspension lines is the CG of HeLion. The obtained CG location leads to the determination of six parameters (category A in Table 3).

Measurement of moment of inertia. The trifilar pendulum method, which is introduced in Ref. 22, is employed to obtain numerical values of the moments of inertia of HeLion. HeLion is suspended by three flexible lines, which are parallel to a body-frame axis and with equal length. The three suspending points and CG are in the same plane, which is perpendicular to the selected body-frame axis. HeLion is then swung around the body-frame axis, and the recorded torsional oscillation period is used to compute the moment of inertia (category B in Table 3).

Airfoil deflection test. This test aims at determining the parameters related to the Bell–Hiller mixer. For both longitudinal and lateral directions, three experiments (similar to Ref. 23) have been conducted.

Table 3. Parameters determined in ground tests

Parameter	Physical Meaning	Category
$D_{hf} = 0.751 \text{ m}$	Horizontal stabilizer location behind the CG	A
$D_{tr} = 1.035 \text{ m}$	Tail rotor hub location behind the CG	A
$D_{vf} = 0.984 \text{ m}$	Vertical stabilizer location behind the CG	A
$H_{mr} = 0.337 \text{ m}$	Main rotor hub location above the CG	A
$H_{tr} = 0.172 \text{ m}$	Tail rotor hub location above the CG	A
$H_{vf} = 0.184 \text{ m}$	Vertical stabilizer location above the CG	A
$J_{xx} = 0.251 \text{ kg}\cdot\text{m}^2$	Rolling moment of inertia	B
$J_{yy} = 0.548 \text{ kg}\cdot\text{m}^2$	Pitching moment of inertia	B
$J_{zz} = 0.787 \text{ kg}\cdot\text{m}^2$	Yawing moment of inertia	B
$A_{lon} = 0.210 \text{ rad}$	Linkage gain ratio of θ_{cyc, a_s} to δ_{lon}	C
$B_{lat} = 0.200 \text{ rad}$	Linkage gain ratio of θ_{cyc, b_s} to δ_{lat}	C
$C_{lon} = 0.560 \text{ rad}$	Linkage gain ratio of stabilizer bar cyclic change to δ_{lon}	C
$D_{lat} = 0.570 \text{ rad}$	Linkage gain ratio of stabilizer bar cyclic change to δ_{lat}	C
$K_{sb} = 1$	Ratio of θ_{cyc, a_s} (or θ_{cyc, b_s}) to c_s (or d_s)	C
$K_I K_a = 8.499 \text{ rad}$	Lumped result of integral gain K_I and scaling K_a	D
$K_P K_a = 1.608 \text{ rad}$	Lumped result of proportional gain K_P and scaling factor K_a	D
$K_{col} = -0.165 \text{ rad}$	Ratio of θ_{col} to δ_{col}	D
$K_{ped} = 1$	Ratio of θ_{ped} to $\bar{\delta}_{ped}$	D
$\theta_{col, 0} = 0.075 \text{ rad}$	Offset of θ_{col} when δ_{col} is zero	D
$\theta_{ped, 0} = 0.143 \text{ rad}$	Offset of θ_{ped} when $\bar{\delta}_{ped}$ is zero	D

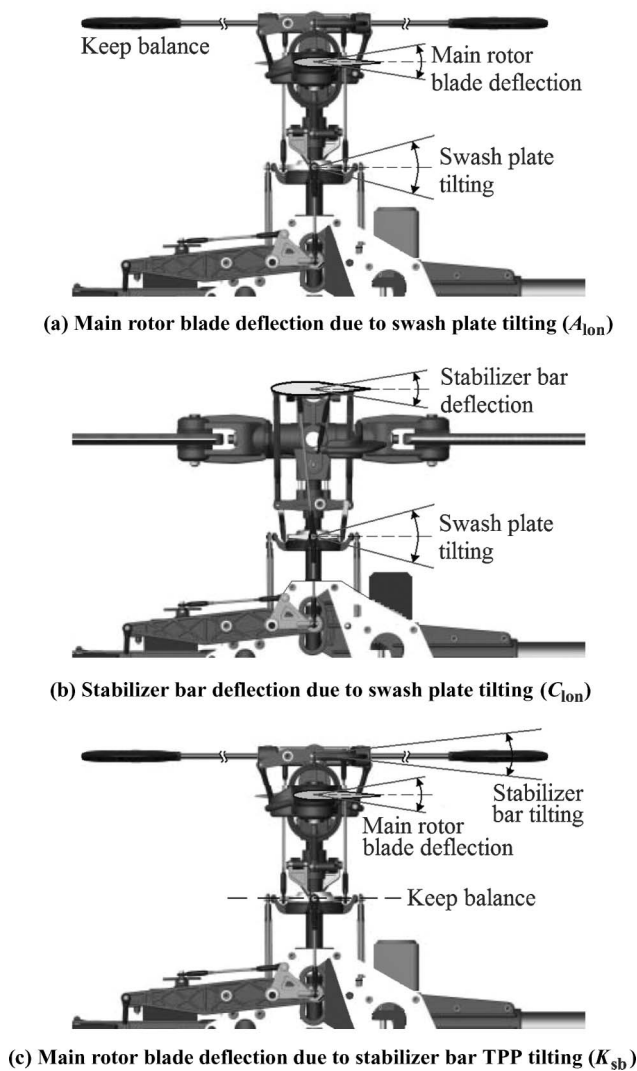


Fig. 3. Airfoil deflection test illustration.

Taking the longitudinal direction as an example, the experiment procedure is depicted in Fig. 3. Three parameters, i.e., A_{10n} , C_{10n} , and K_{sb} , can be determined.

1) Determination of A_{10n} (see Fig. 3(a)) consists of three steps: (a) adjust and maintain the stabilizer bar to be level to the X axis of the body frame, (b) inject δ_{10n} to tilt the swash plate longitudinally, and (c) record $\theta_{cyc,as}$ (the cyclic pitch deflection of the main rotor blade). A_{10n} is the ratio of $\theta_{cyc,as}$ to δ_{10n} .

2) For C_{10n} (see Fig. 3(b)), the experiment follows: (a) adjust the stabilizer bar to be level to the X axis of the body frame, (b) keep the cyclic pitch of the main rotor blade unchanged, (c) inject δ_{10n} to tilt the swash plate longitudinally, and (d) record the deflection of the stabilizer bar paddle. C_{10n} is the ratio of the paddle deflection to δ_{10n} .

3) For K_{sb} (see Fig. 3(c)), the experiment consists of (a) adjust the stabilizer bar to be level to the X axis of the body frame, (b) keep the swash plate balanced, and (c) manually change the stabilizer bar flapping angle c_s and record the corresponding change in $\theta_{cyc,as}$. K_{sb} is the ratio of $\theta_{cyc,as}$ to c_s .

The same experiments are applied to the lateral direction to identify B_{lat} and D_{lat} . Another numerical result of K_{sb} can be obtained via a lateral deflection experiment. The two results are almost identical, which is consistent with the expectation that K_{sb} is a Bell-Hiller mixer setting

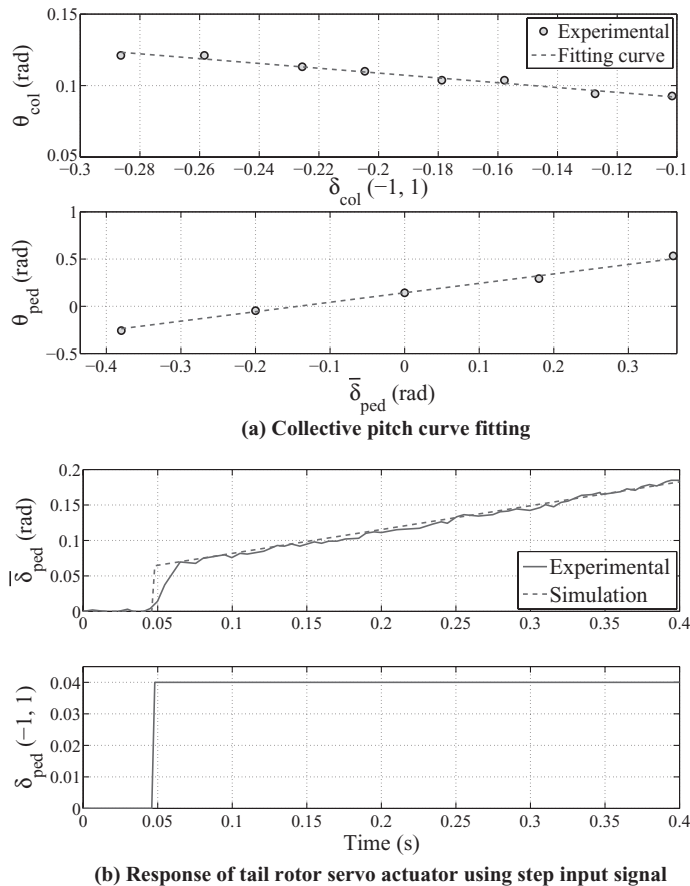


Fig. 4. Results of collective pitch curve examination.

that is strictly symmetrical to both directions. The results obtained in the airfoil deflection test are grouped into category C in Table 3.

Collective pitch curve examination. The collective pitch curve experiments are applied to both the main rotor and the tail rotor. These tests aim to determine the relationship between the servo actuator input δ_{col} ($\bar{\delta}_{ped}$ for the tail rotor) and the blade collective pitch angle θ_{col} (θ_{ped} for the tail rotor).

For the main rotor, seven input values within the effective working range of δ_{col} are chosen and their corresponding collective pitch angles are recorded. The linear relationship is reflected by Fig. 4. The least-square curve-fitting method is then used to determine K_{col} and $\theta_{col,0}$.

For the tail rotor, owing to the existence of the yaw rate feedback controller, the dynamics from δ_{ped} to θ_{ped} is divided into two parts (i.e., $\bar{\delta}_{ped}$ to θ_{ped} and δ_{ped} to $\bar{\delta}_{ped}$). The former is a linear relationship shown in Fig. 4. The numerical results for the associated parameters K_{ped} and $\theta_{ped,0}$ can be easily obtained. The latter part focuses on estimating the parameters of the amplification circuit, and the proportional/integral gains of the feedback controller. A step input signal is injected to δ_{ped} , and the associated response of $\bar{\delta}_{ped}$ shown in Fig. 4 is recorded by a potentiometer. The results for the lumped $K_p K_a$ and $K_I K_a$ can be obtained using least-square curve fitting. Note that the values of K_p , K_I , and K_a are determined after K_a is identified via flight experiment (to be discussed later). Category D of Table 3 summarizes the parameters obtained in the collective pitch curve examination.

Table 4. Airfoil features of HeLion

Airfoil	Airfoil Shape	Reynolds Number	Aspect Ratio
Main rotor blade	NACA 0012	3.07×10^5	11.37
Tail rotor blade	NACA 0012	1.21×10^6	4.41
Stabilizer bar	NACA 0012	2.25×10^5	1.37
Horizontal stabilizer	Flat plate	1.02×10^5	3.11
Vertical stabilizer	Flat plate	0.92×10^5	2.52

Estimation based on the wind tunnel data

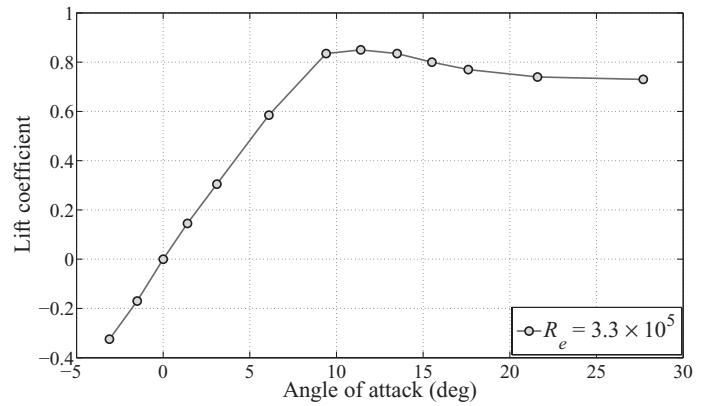
Wind tunnel data are essential to determine the lift curve slopes (and drag coefficient) for various airfoils, including (1) main rotor blade, (2) tail rotor blade, (3) stabilizer bar paddle, (4) horizontal stabilizer, and (5) vertical stabilizer. Although it is impractical for us to conduct wind tunnel experiments, numerous wind tunnel databases are available in the open literature and can be adopted as the baseline for parameter estimation in this step. There are three factors in our wind tunnel data selection: (1) *airfoil shape*: the most fundamental baseline for evaluating the suitability of the wind tunnel data, (2) *Reynolds number* (R_e): miniature helicopters commonly work in regimes with a low Reynolds number ($<10^6$), and (3) *aspect ratio*: with the same airfoil and Reynolds number, low aspect ratio can greatly reduce the lift coefficient.

Table 4 provides the three features for each of the involved airfoils. Reynolds number computation can be found in many fluid dynamics texts. Two key points of the computation should be highlighted. First, for the main rotor blade, tail rotor blade, and stabilizer bar, the reference points are located at the middle of these airfoils, with the chord lengths of 0.353, 0.064, and 0.272 m, respectively. Second, the horizontal and vertical stabilizers are assumed to be isosceles triangles. The traveled length of the calculated Reynolds number is taken to be the half height of the associated isosceles triangle. Based on Table 4, the wind tunnel data reported in Refs. 24–26 (as depicted in Figs. 5 and 6) are chosen. The determined parameters include (1) C_{D0} (0.01), (2) $C_{l_{\alpha, hf}}$ (2.85 rad^{-1}), (3) $C_{l_{\alpha, mr0}}$ (5.73 rad^{-1}), (4) $C_{l_{\alpha, sb0}}$ (2.08 rad^{-1}), (5) $C_{l_{\alpha, tr0}}$ (2.08 rad^{-1}), and (6) $C_{l_{\alpha, vf}}$ (2.85 rad^{-1}). It is noted that $C_{l_{\alpha, mr0}}$, $C_{l_{\alpha, sb0}}$, and $C_{l_{\alpha, tr0}}$ are temporary estimations of these lift curve slopes. They will be further tuned in the last step of the parameter determination procedure, i.e., fine-tuning.

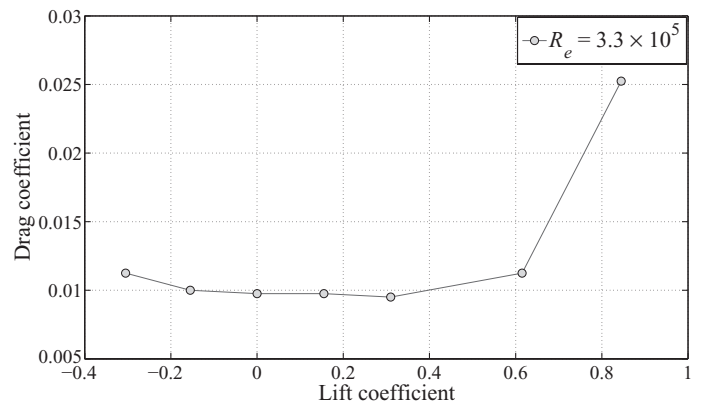
Flight test

The approach of system identification is used in this step. The primary aim of conducting flight test is to determine more unknown parameters and validate some parameters obtained in the previous steps. Note that only the data collected in hover and near hover conditions are utilized. The main reason is that in flight conditions with moderate speed and aggressiveness, it is generally difficult for a human pilot to perturb a miniature rotorcraft persistently while maintaining the desired trimmed status. The following two flight experiments have been performed in this step.

Pirouette flight. Pirouette experiment requires HeLion to follow a 10-m-radius circle, with the nose pointing to the center of the circle while its yaw rate is kept constant. According to Eq. (49), K_a is the ratio between the yaw rate and the input δ_{ped} . Based on the result shown in Fig. 7, K_a (-3.85 rad) is determined and K_1 (2.2076) and K_p (0.4177) are further isolated from the lumped results given in the category D of Table 3.



(a) Wind tunnel result for the lift curve slope of the main rotor blade (aspect ratio = 6)



(b) Wind tunnel result for the drag coefficient of the main rotor blade (aspect ratio = 6)

Fig. 5. Wind tunnel data (part 1).

Frequency-domain identification. In frequency-domain identification, frequency-sweep technique, which is widely used in both full-scale and small-scale rotorcraft modeling, is adopted. The literature (see, e.g., Refs. 1, 5, 6, 27) shows that for small-scale helicopters this technique has the highest fidelity in modeling the linear angular rate dynamics at hover condition. Thus, Eqs. (7), (47), and (48) are combined to form the following state-space dynamic structure:

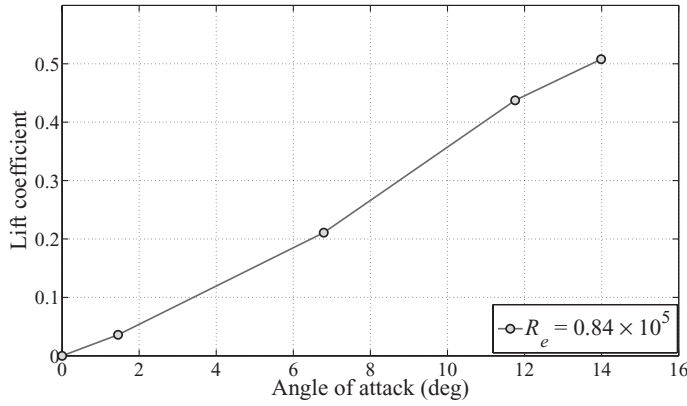
$$\dot{\mathbf{x}} = \begin{bmatrix} 0 & 0 & 0 & L_{b_s} \\ 0 & 0 & M_{a_s} & 0 \\ 0 & -1 & \frac{1}{\tau_{mr} + \tau_{sb}} & \frac{\tau_{mr} A_{b_s}}{\tau_{mr} + \tau_{sb}} \\ -1 & 0 & \frac{\tau_{mr} B_{a_s}}{\tau_{mr} + \tau_{sb}} & \frac{1}{\tau_{mr} + \tau_{sb}} \end{bmatrix} \mathbf{x} + \begin{bmatrix} 0 & 0 \\ 0 & 0 \\ 0 & A_{lon,eff} \\ B_{lat,eff} & 0 \end{bmatrix} \mathbf{u} \quad (51)$$

and

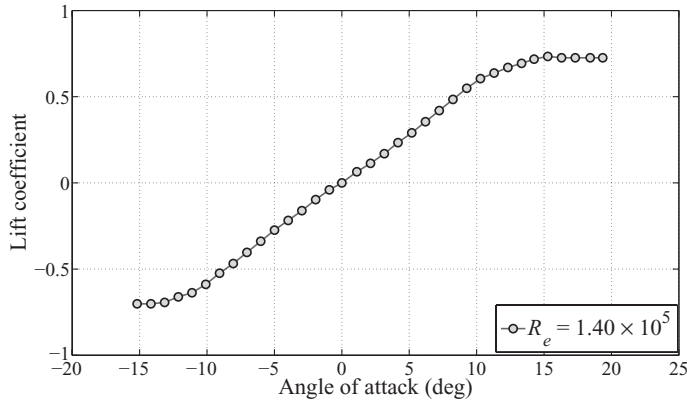
$$\mathbf{y} = \begin{bmatrix} 1 & 0 & 0 & 0 \\ 0 & 1 & 0 & 0 \end{bmatrix} \mathbf{x} \quad (52)$$

where $\mathbf{x} = (p \ q \ a_s \ b_s)^T$, $\mathbf{u} = (\delta_{lat} \ \delta_{lon})^T$, and $\mathbf{y} = (p \ q)^T$. L_{b_s} and M_{b_s} are lumped lateral and longitudinal rotor spring derivatives, $A_{lon,eff}$ and $B_{lat,eff}$ are the effective time constants of the complete main rotor flapping dynamics. They are respectively given by

$$L_{b_s} = \frac{mg H_{mr} + K_{\beta}}{J_{xx}}, \quad M_{b_s} = \frac{mg H_{mr} + K_{\beta}}{J_{yy}} \quad (53)$$



(a) Wind tunnel data related to the stabilizer bar and tail rotor blade (aspect ratio = 1)



(b) Wind tunnel data related to the flat-plate horizontal and vertical stabilizers (aspect ratio = 2)

Fig. 6. Wind tunnel data (part 2).

and

$$A_{lon,eff} = \frac{A_{lon} + K_{sb} C_{lon}}{\tau_{mr} + \tau_{sb}}, \quad B_{lat,eff} = \frac{B_{lat} + K_{sb} D_{lat}}{\tau_{mr} + \tau_{sb}} \quad (54)$$

It is noted that parameters A_{lon} , B_{lat} , C_{lon} , D_{lat} , K_{sb} , J_{xx} , and J_{yy} have been determined earlier in the ground tests. Among them, the first five parameters are related to the mechanical design of the Bell–Hiller mixer and can be directly used in the following identification process, whereas the validity of the latter two parameters is to be further examined.

The identification procedure is assisted by an identification toolkit called CIFER, developed by NASA Ames Research Center. Specifically,

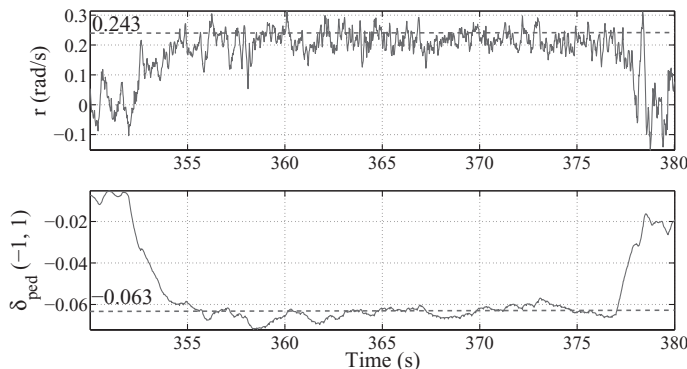
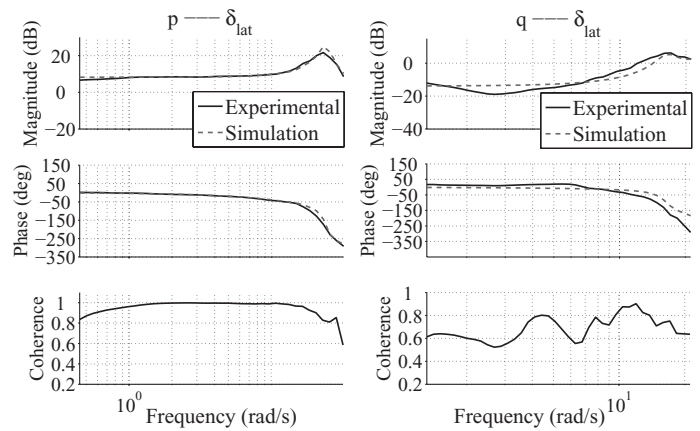
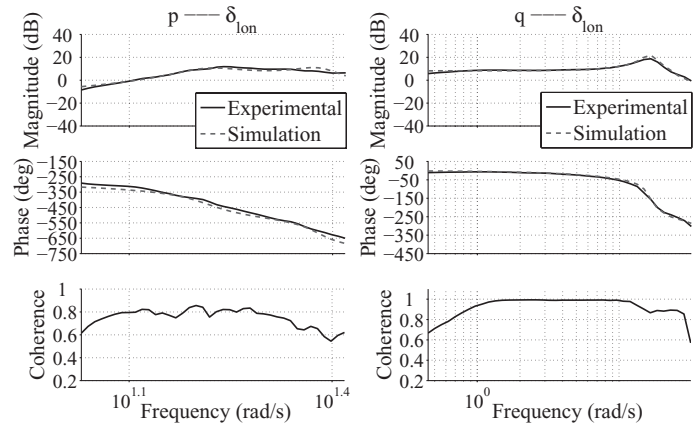


Fig. 7. Pirouette flight test for K_a determination.



(a) Frequency-sweep input (δ_{lat})



(b) Frequency-sweep input (δ_{lon})

Fig. 8. Response comparison using frequency-sweep input.

the frequency-sweep signal, which is detailed in Ref. 1, is manually performed for each of the input channels at the hover condition, and the resulting time-history data are recorded and further converted to frequency-domain responses. The coherence value γ_{xy}^2 of the frequency-domain data is an important index to indicate whether the system can be well characterized as a linear process at the frequency of interest. Following Ref. 1, the threshold value is set as 0.6. Next CIFER identifies the parameters of Eq. (51) by minimizing the following average cost function:

$$J_{ave} = \frac{1}{n_{TF}} \sum_{s=1}^{n_{TF}} \left\{ \sum_{\omega_1}^{\omega_{n\omega}} 2.4964 (1 - e^{-\gamma_{xy}^2})^2 [(|\hat{F}_c| - |F|)^2 + 0.01745(\angle \hat{F}_c - \angle F)^2] \right\}_s \quad (55)$$

where n_{TF} is the number of the frequency-response pairs, ω_1 and $\omega_{n\omega}$ are starting and ending frequencies, F and F_c are desired and practical frequency-response estimates, and $| \cdot |$ and \angle represent amplitude (dB) and phase (deg) at a specific frequency point.

The frequency-domain matching is depicted in Fig. 8. The associated J_{ave} is 85, which reflects a good level of accuracy, according to the guideline (denoted in Ref. 1) that J_{ave} should be less than 100. The identified parameter values are listed in Table 5, together with two statistics provided by CIFER for evaluating the identification fidelity, namely (1)

Table 5. Parameters identified using CIFER system identification toolkit

Parameter	CR Bound (%)	Insensitivity (%)	Physical Meaning
$L_{b_s} = 583.50 \text{ s}^{-2}$	1.88	0.69	Lateral rotor spring derivative
$M_{a_s} = 265.30 \text{ s}^{-2}$	1.53	0.64	Longitudinal rotor spring derivative
$\tau_{mr} + \tau_{sb} = 0.299 \text{ s}$	2.68	1.25	Effective rotor time constant
$\frac{\tau_{mr} A_{b_s}}{\tau_{mr} + \tau_{sb}} = 2.223 \text{ s}^{-1}$	2.51	5.26	Coupling effect of rotor flapping dynamics
$\frac{\tau_{mr} B_{a_s}}{\tau_{mr} + \tau_{sb}} = 2.448 \text{ s}^{-1}$	5.00	2.07	Coupling effect of rotor flapping dynamics
$K_\beta = 114.05 \text{ N}\cdot\text{m}$	NA	NA	Main rotor spring constant

Cramer–Rao (CR) bound (less than 20%), which indicates the level of the parameter identifiability and (2) insensitivity (less than 10%), which indicates whether the parameter is important to the selected model structure, as described in Ref. 1. Table 5 indicates that all the parameters identified using CIFER are accurate. Interested readers are referred to Ref. 6 for a similar implementation on an X-Cell 60–based UAV helicopter.

We further evaluate the dynamic modes of the coupled multiple-input-multiple-output system expressed in Eq. (51). The identified result indicates that the eigenvalues are (1) $-1.64 \pm 23.89i$: lightly damped roll mode (with the damping ratio of 0.07 and the natural frequency of 23.94 rad/s) that corresponds to the coupled rotor–fuselage dynamics in rolling motion and (2) $-1.70 \pm 16.34i$: lightly damped pitch mode (with the damping ratio of 0.10 and the natural frequency of 16.43 rad/s) that corresponds to the coupled rotor–fuselage dynamics in pitching motion. The two pairs of eigenvalues are inherently stable. Owing to this reason, the frequency-domain matching and the identified parameters are generally accurate.

Based on the obtained intermediate results, the following four steps have been performed:

1) *Validation of J_{xx} and J_{yy} .* Equation (53) shows that

$$\frac{L_{b_s}}{M_{a_s}} = \frac{J_{yy}}{J_{xx}} \quad (56)$$

Based on the results obtained, the actual ratios of L_{b_s}/M_{a_s} and J_{yy}/J_{xx} are 2.199 and 2.185, respectively. The difference of only 0.6% illustrates the validity of the previously determined values of J_{xx} and J_{yy} .

2) *K_β identification.* Based on Table 3 (trifilar pendulum experiment result), Table 5, and Eq. (53), K_β can be calculated in terms of both rolling and pitching responses. The two numerical values are 114.76 and 113.33, respectively. Their average, i.e., 114.05, is then used.

3) *Initial verification of $C_{l\alpha, mr}$ and $C_{l\alpha, sb}$.* The two lift curve slopes, which are estimated previously using the wind tunnel data, generate another estimate for $\tau_{mr} + \tau_{sb}$. Following Eqs. (40) and (43), $\tau_{mr} + \tau_{sb}$ has the value of 0.275. The small deviation between the CIFER system identification result (see Table 5) and the wind tunnel–based result indicates the good validity of the aforementioned temporary estimations of these two lift curve slopes ($C_{l\alpha, mr0}$ and $C_{l\alpha, sb0}$). However, since the system identification method only gives us the sum of τ_{mr} and τ_{sb} , the specific values of $C_{l\alpha, mr}$ and $C_{l\alpha, sb}$ cannot be determined at this stage.

4) *Analysis of coupling effect in rotor flapping.* The validity of the identified coupling derivatives in Table 5 is verified by the close frequency matching, low CR bound, and low Insensitivity. However, it cannot be predicted by the theoretical calculation resulting from Eq. (46). This deficiency partially results from the simplified model structure.

Fine-tuning

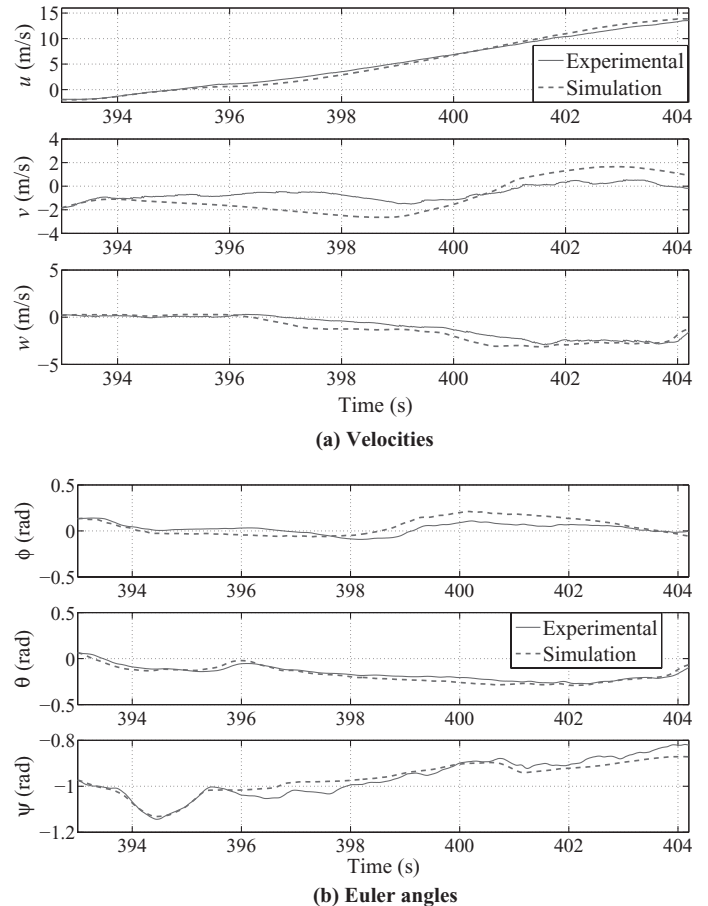
The main aim of the last parameter identification step is to determine the three lift curve slopes $C_{l\alpha, mr}$, $C_{l\alpha, sb}$, and $C_{l\alpha, tr}$ as well as A_{b_s} and B_{a_s} . The general idea is to examine the balanced relationship in the ideal hovering condition. The following are noted:

1) 10 equations, i.e., the rigid-body dynamics in Eqs. (6) and (7), the main-rotor thrust calculation in Eqs. (9) and (10), and the tail-rotor thrust calculation in Eqs. (22) and (23), are involved,

2) 10 parameters (ϕ_{trim} , θ_{trim} , $a_{s, trim}$, $b_{s, trim}$, $T_{mr, trim}$, $T_{tr, trim}$, $v_{i, mr, trim}$, $v_{i, tr, trim}$, $C_{l\alpha, mr}$, and $C_{l\alpha, tr}$), in which the subscript trim represents the trimmed values at hover, will be determined, and

3) The trimmed values for δ_{col} and δ_{ped} (-0.1746 and 0 for HeLion), which can be easily obtained through a manual experiment, are necessary to form the balanced relationship.

With proper initialization (e.g., utilizing the approximation of $T_{mr} = mg$ to generate the associated $v_{i, mr}$, T_{tr} and $v_{i, tr}$) and using an appropriate numerical searching algorithm (in our case, the trust-region dogleg method integrated in MATLAB[®] is adopted), the nonlinear equations can quickly converge to an expected result. More specifically, we have ϕ_{trim} (0.039 rad), θ_{trim} (0.001 rad), $a_{s, trim}$ (-0.001 rad), $b_{s, trim}$ (0.005 rad), $T_{mr, trim}$ (96.766 N), $T_{tr, trim}$ (4.188 N), $v_{i, mr, trim}$ (4.90 m/s), $v_{i, tr, trim}$ (5.62 m/s), $C_{l\alpha, mr}$ (5.52 rad^{-1}), and $C_{l\alpha, tr}$ (2.82 rad^{-1}). Based on the


Fig. 9. Forward flight test results.

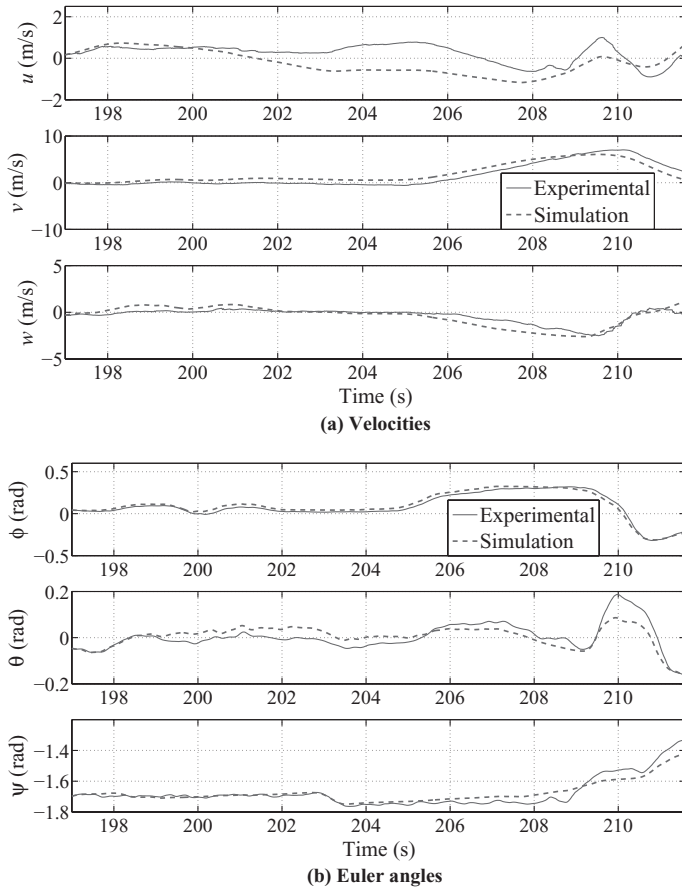


Fig. 10. Sideslip flight test results.

determined $C_{l\alpha, mr}$, the rotor time constant τ_{mr} can be obtained via Eq. (43). Combined with the identification result given in Table 5, we can compute τ_{sb} and finally obtain $C_{l\alpha, sb}$ (2.72 rad^{-1}), A_{bs} (9.720 s^{-1}), and B_{as} (10.704 s^{-1}).

The above five steps form the parameter determination procedure. Here, a brief discussion on model nonlinearity is presented. It can be noted that in our minimum-complexity model, the structure and parameters involved do not vary with respect to the different flight conditions. However, the nonlinearity is an inherent property of the model, which resides mainly in both the translational and the rotational dynamics. To illustrate this point, model linearization has been conducted under three representative flight conditions (with body-frame longitudinal velocity of 0, 6, and 12 m/s). The body-frame X-axis speed force damping derivative, denoted by X_u , has the values -0.0335 , -0.0812 , and -0.1620 for the above-mentioned three flight conditions. Similarly, for the Z-axis speed force damping derivative Z_w , the numerical results are, respectively, -0.7374 , -1.1174 , and -1.5439 . The nonlinearity can be observed in the change in the numerical values (and corresponding inherent stability) with respect to different speeds.

Model Validation

In this section, an evaluation on the model fidelity is performed. Under manual control, three representative flight tests have been conducted, i.e., (1) a high-speed forward flight for which HeLion is commanded to start with stable hover, and then gradually accelerate to a preset forward velocity of 14 m/s based on a step-like input signal, (2) a sideslip flight for which HeLion starts with stable hover, then accelerates to a moderate

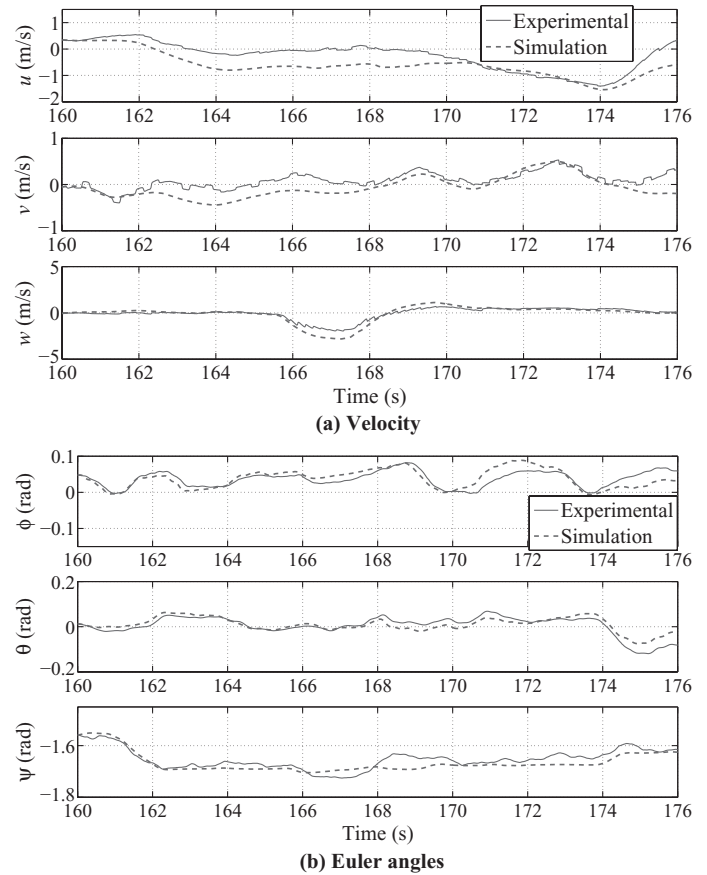


Fig. 11. Heave flight test results.

lateral velocity at about 7 m/s, and subsequently decelerates to reach the near hovering condition again, and (3) a heave flight test under which HeLion starts again from stable hover before ascending until its heave velocity reaches 2 m/s, and then decelerates to hover at a higher point. Based on the same inputs, the experimental and simulation responses in terms of the body-frame velocities and Euler angles are compared. The results shown in Figs. 9–11 indicate that the maximum deviations for velocity and Euler angles are only 1.5 m/s and 0.1 rad, respectively. Such coincidences prove that the model can capture the flight dynamics of HeLion over a fairly wide envelope. The aforementioned deviations are mainly caused by wind gusts and unmodeled flight dynamics or aerodynamics. The resulting inaccuracy can be overcome by a properly developed automatic control system.

Conclusions

1) A comprehensive modeling process that is particularly suitable for miniature unmanned rotorcraft has been introduced. Both model structure and parameter determination have been detailed.

2) A suitable trade-off between model fidelity and structural complexity has been made. The model contains only four flight dynamics components. Complex aerodynamics related to aerodynamic force and rotor flapping are not involved in the model. The close match between the simulation responses and the experimental data illustrates that the model structure is suitable for miniature unmanned helicopters.

3) A five-step parameter determination process has been proposed to obtain the unknown parameters. This process is an integration of first-principles modeling approach and system identification. Most of the

parameters can be determined via direct measurement and simple ground tests. Some wind tunnel data available online can provide good initial estimates of the parameters related to aerodynamic lift and drag, and the determined values of these parameters only vary slightly. CIPHER-based system identification has been proven to be efficient in (1) identifying parameters that are difficult to determine using a first-principles approach and (2) intermediate validation for some parameters.

4) A miniature UAV helicopter, HeLion, is used as an example. The modeling method, particularly the parameter determination process, can be applied to model any miniature rotorcraft UAV.

References

- ¹Tischler, M. B., and Remple, R. K., *Aircraft and Rotorcraft System Identification—Engineering Methods with Flight Test Examples*, AIAA Educational Series, AIAA, Reston, VA, 2006, Chaps. 1, 5, 11, and 15.
- ²Morris, J. C., Nieuwstadt, M., and Bendotti, P., “Identification and Control of a Model Helicopter in Hover,” Proceedings of American Control Conference, Baltimore, MD, June 29–July 1, 1994, pp. 1238–1242.
- ³Shim, D. H., Kim, H. J., and Sastry, S., “Control System Design for Rotorcraft-Based Unmanned Aerial Vehicle Using Time-Domain System Identification,” Proceedings of the 2000 IEEE Conference on Control Applications, Anchorage, AK, September 25–27, 2000, pp. 808–813.
- ⁴Mettler, B., Tischler, M. B., and Kanade, T., “System Identification of Small-Size Unmanned Helicopter Dynamics,” American Helicopter Society 55th Annual Forum Proceedings, Montreal, Canada, May 25–27, 1999, pp. 1706–1717.
- ⁵Cheng, R. P., Tischler, M. B., and Schulein, G. J., “Rmax Helicopter State-Space Model Identification for Hover and Forward-flight,” *Journal of the American Helicopter Society*, Vol. 51, (2), April 2006, pp. 202–210.
- ⁶Mettler, B., *Identification, Modeling and Characteristics of Miniature Rotorcraft*, Kluwer Academic Publishers, Boston, MA, 2002, Chaps. 3–5.
- ⁷Padfield, G. D., *Helicopter Flight Dynamics: The Theory and Application of Flying Qualities and Simulation Modeling*, AIAA Education Series, AIAA, Reston, VA, 1996, Chap. 3.
- ⁸Leishman, J. G., *Principles of Helicopter Aerodynamics*, Cambridge University Press, New York, NY, 2002, Chap. 6.
- ⁹Bramwell, A. R. S., *Bramwell’s Helicopter Dynamics*, AIAA Educational Series, AIAA, Reston, VA, 2001, Chap. 5.
- ¹⁰Gavrilets, V., Mettler, B., and Feron, E., “Nonlinear Model for a Small-Size Acrobatic Helicopter,” AIAA-2001-4333, AIAA Guidance, Navigation, and Control Conference and Exhibit Proceedings, Montreal, Canada, August 6–9, 2001.
- ¹¹Kim, S. K., and Tilbury, D. M., “Mathematical Modeling and Experimental Identification of an Unmanned Helicopter Robot with Flybar Dynamics,” *Journal of Robotic Systems*, Vol. 21, (3), March 2004, pp. 95–116.
- ¹²Civita, M. L., Messner, W., and Kanade T., “Modeling of Small-Scale Helicopters with Integrated First-Principles and Integrated System Identification Techniques,” American Helicopter Society 58th Annual Forum Proceedings, Montreal, Canada, May 25–27, 2002, pp. 2505–2516.
- ¹³Harris, F. D., “Articulated Rotor Blade Flapping Motion at Low Advance Ratio,” *Journal of the American Helicopter Society*, Vol. 17, (1), January 1972, pp. 41–48.
- ¹⁴Heffley, R. K., and Mnich, M. A., “Minimum-Complexity Helicopter Simulation Math Model,” NASA CR 177476, April 1988.
- ¹⁵Mettler, B., Tischler, M. B., and Kanade, T., “System Identification Modeling of a Small-Scale Unmanned Rotorcraft for Control Design,” *Journal of the American Helicopter Society*, Vol. 47, (1), January 2002, pp. 50–63.
- ¹⁶Munzinger, C., “Development of a Real-Time Flight Simulator for an Experimental Model Helicopter,” M.S. Thesis, School of Aerospace Engineering, Georgia Institute of Technology, Atlanta, GA, 1998.
- ¹⁷Prouty, R. W., *Helicopter Performance, Stability, and Control*, R. E. Krieger Publishing Company, Malabar, FL, 1990, Chaps. 2–6.
- ¹⁸Tischler, M. B., and Cauffman, M. G., “Frequency-Response Method for Rotorcraft System Identification: Flight Application of BO-105 Coupled Rotor/Fuselage Dynamics,” *Journal of the American Helicopter Society*, Vol. 37, (3), July 1992, pp. 3–17.
- ¹⁹Stevens, B. L., and Lewis, F. L., *Aircraft Control and Simulation*, 2nd ed., John Wiley & Sons, Hoboken, NJ, 2003, Chap. 1.
- ²⁰Johnson, W., *Helicopter Theory*, Dover Publications, Mineola, NY, 1994, Chap. 2.
- ²¹Heffley, R. K., Bourne, S. M., Curtiss, H. C., Hindson, W. S., and Hess, R. A., “Study of Helicopter Roll Control Effectiveness Criteria,” NASA CR 177404, April 1986.
- ²²Himmelblau, H., and Rubin, S., “Vibration of a Resiliently Supported Rigid Body,” *Shock and Vibration Handbook*, edited by C. Harris, McGraw-Hill, New York, NY, 1996, Chap. 3, pp. 1–10.
- ²³Hald, U. B., Hesselbek, M. V., and Siegumfeldt, M., “Nonlinear Modeling and Optimal Control of a Miniature Autonomous Helicopter,” M.S. Thesis, Department of Control Engineering, Aalborg University, Aalborg, Denmark, 2006.
- ²⁴Jacobs, E. N., and Sherman, A., “Airfoil Section Characteristics as Affected by Variations of the Reynolds Number,” NACA Report 586, 1937.
- ²⁵Pelletier, A., and Mueller, T. J., “Low Reynolds Number Aerodynamics of Low-Aspect-Ratio, Thin/Flat/Cambered-Plate Wings,” *Journal of Aircraft*, Vol 37, (5), September 2000, pp. 825–832.
- ²⁶Sathaye, S. S., “Lift Distributions on Low Aspect Ratio Wings at Low Reynolds Numbers,” M.S. Thesis, Department of Mechanical Engineering, Worcester Polytechnic Institute, Worcester, MA, 2004.
- ²⁷Ham, J. A., Gardner, C. K., and Tischler, M. B., “Flight-Testing and Frequency-Domain Analysis for Rotorcraft Handling Qualities,” *Journal of the American Helicopter Society*, Vol. 40, (2), April 1995, pp. 28–38.